Original Article | **Open Access**

Extracellular Vesicles and Circulating Nucleic Acids

Li *et al. Extracell Vesicles Circ Nucleic Acids.* 2026;7:1825-45 **DOI:**10.20517/evcna.2026.146

Engineered Panax notoginseng nanovesicles enhance peptide delivery in intracerebral hemorrhage

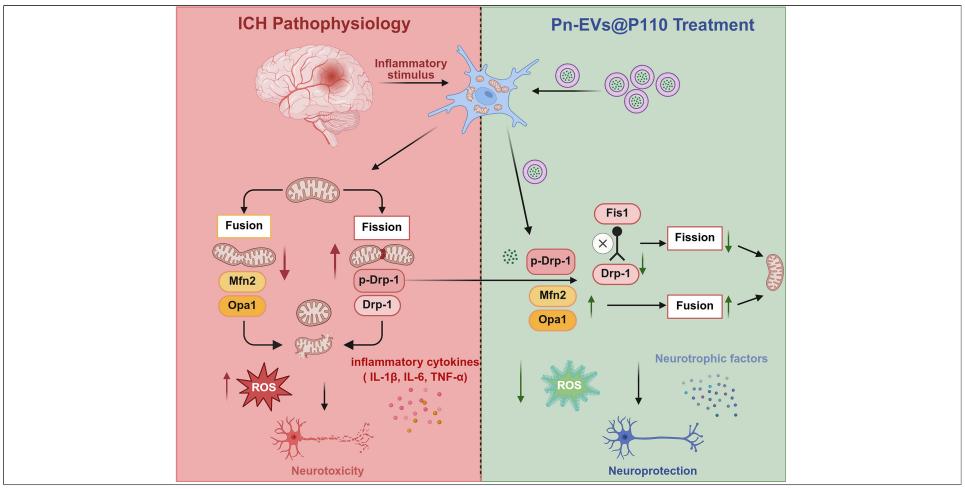
Yanan Li[1,#], Bin Xu[1,#], Wenxue, Tao Zhang[2], Changshui Wang[2], Beibei Chen[3], Pei Jiang[2]

Keywords:
Panax notoginseng-derived nanovesicles, extracellular vesicles, engineered vesicles, peptide delivery, intracerebral hemorrhage, microglia, mitochondrial dynamics, neuroinflammation

Citation: Li Y, Xu B, Sun W, Zhang T, Wang C, Chen B, Jiang P. Engineered *Panax notoginseng* nanovesicles enhance peptide delivery in intracerebral hemorrhage. *Extracell Vesicles Circ Nucleic Acids.* 2026;7:1825-45. https://dx.doi.org/10.20517/evcna.2026.146

Received: 8 Jul 2026 **First Decision:** 17 Aug 2026 **Revised:** 14 Sep 2026 **Accepted:** 18 Sep 2026 **Published:** 16 Oct 2026

Academic Editor: Yoke Peng Loh
Copy Editor: Ting-Ting Hu
Production Editor: Ting-Ting Hu



Abstract

Aim: Peptide therapeutics for intracerebral hemorrhage (ICH) are often limited by rapid degradation and insufficient brain exposure following systemic administration. This study aimed to evaluate whether *Panax notoginseng*-derived extracellular vesicle-like nanovesicles (Pn-EVs) could serve as carriers to improve the delivery and therapeutic efficacy of the mitochondrial fission inhibitor P110 in experimental ICH.

Methods: Pn-EVs were isolated from *Panax notoginseng* by differential ultracentrifugation and associated with P110 through sonication to generate Pn-EVs@P110. Association efficiency, stability, and *in vitro* release behavior were evaluated. Biodistribution was assessed by fluorescence imaging in collagenase-induced ICH mice. Neurological function, hematoma volume, cerebral edema, neuronal injury, microglial activation, inflammatory responses, oxidative stress, mitochondrial dynamics-related proteins, and transcriptomic and metabolomic alterations were analyzed to evaluate therapeutic effects and potential mechanisms.

[1]College of Marine Life Sciences, Ocean University of China, Qingdao 266003, Shandong, China.
[2]Translational Pharmaceutical Laboratory, Jining No. 1 People's Hospital, Shandong First Medical University, Jining 272000, Shandong, China.
[3]School of Life Science and Bioengineering, Jining University, Jining 273155, Shandong, China.
[#]These authors contributed equally to this work.

Correspondence to: Dr. Beibei Chen, School of Life Science and Bioengineering, Jining University, Jining 273155, Shandong, China. E-mail: beibei.chen@unswalumni.com; Prof. Pei Jiang, Translational Pharmaceutical Laboratory, Jining No. 1 People's Hospital, Shandong First Medical University, Jining 272000, Shandong, China. E-mail: jiangpeicsu@sina.com

Results: Pn-EVs@P110 exhibited an association efficiency exceeding 80%, stable physicochemical properties, and sustained release of P110 *in vitro*. Fluorescence imaging demonstrated accumulation of vesicle-associated signals in the injured brain after intravenous administration. Compared with free P110, Pn-EVs@P110 significantly improved neurological outcomes, reduced hematoma volume and brain edema, and attenuated neuronal loss in ICH mice. These effects were associated with attenuated microglial activation, lower levels of pro-inflammatory cytokines and oxidative stress markers, and restoration of mitochondrial dynamics-related alterations. Multi-omics analyses further indicated modulation of inflammation- and mitochondrial-related pathways.

Conclusion: Pn-EVs may serve as a biogenic delivery platform that enhances the therapeutic efficacy of P110 in experimental ICH. These findings support the potential application of plant-derived extracellular vesicle-like nanovesicles as peptide delivery vehicles for neurological disorders.

INTRODUCTION

Extracellular vesicles (EVs) have attracted substantial interest as nanoscale delivery systems owing to their intrinsic biocompatibility, membrane stability, and capacity for intercellular communication[1,2]. Their ability to transport proteins, nucleic acids, lipids, and small bioactive molecules across biological barriers has further supported their development as carriers for therapeutic agents in a wide range of diseases[3]. Accordingly, considerable effort has been made toward improving EV cargo loading, targeting specificity, circulation stability, and therapeutic efficacy[4]. Nevertheless, clinical translation remains constrained by low production yield, batch-to-batch variability, cargo retention efficiency, scalable manufacturing, and translational feasibility[5-7]. These limitations have increased interest in alternative EV sources that combine favorable biological properties with scalable and cost-effective production.

Plant-derived extracellular vesicle-like nanovesicles have recently emerged as an attractive alternative to mammalian EVs because of their low immunogenicity, excellent biosafety, abundant availability, and scalable production[8-10]. Beyond functioning as natural nanocarriers, accumulating evidence indicates that plant-derived vesicles possess intrinsic biological activities through their endogenous cargo, including proteins, lipids, RNAs, metabolites, and phytochemicals inherited from their botanical origins[11]. Plant-derived vesicles therefore offer a therapeutic platform that combines cargo delivery with the biological activities of naturally occurring plant components. Recent studies have demonstrated encouraging therapeutic efficacy of plant-derived vesicles in inflammatory diseases, metabolic disorders, intestinal diseases, tissue repair, and neurological injuries, highlighting their growing translational potential[11-13].

Among plant-derived vesicles, those isolated from traditional Chinese medicinal herbs have attracted increasing attention because they may retain the therapeutic characteristics of their source herbs while preserving the intrinsic advantages of EVs[14,15]. *Panax notoginseng* is one of the most widely used medicinal herbs for the treatment of cerebrovascular disorders owing to its well-established anti-inflammatory, antioxidant, neuroprotective, and vasculoprotective properties[16-19]. Emerging evidence further suggests that *Panax notoginseng*-derived extracellular vesicle-like nanovesicles (Pn-EVs) inherit part of these pharmacological characteristics and exhibit favorable biocompatibility and therapeutic potential in experimental disease models[20,21]. Together, these observations indicate that Pn-EVs may function as drug carriers and bioactive therapeutic platforms that contribute to treatment efficacy.

Intracerebral hemorrhage (ICH) is a particularly devastating hemorrhagic stroke subtype associated with high mortality and long-term neurological disability, for which effective pharmacological therapies remain extremely limited[22-25]. Secondary brain injury following ICH is characterized by excessive

neuroinflammation, oxidative stress, metabolic disturbance, and mitochondrial dysfunction, particularly in activated microglia, which collectively contribute to progressive neuronal damage and neurological deterioration[26-30]. Growing evidence identifies dysregulated mitochondrial dynamics as a critical pathological mechanism linking mitochondrial dysfunction to inflammatory amplification after ICH[30,31]. In particular, excessive mitochondrial fission mediated by the interaction between dynamin-related protein 1 (Drp1) and mitochondrial fission protein 1 (Fis1) promotes mitochondrial fragmentation, reactive oxygen species (ROS) production, and pro-inflammatory microglial activation[32,33]. P110 is a selective peptide inhibitor that interferes with the pathological Drp1-Fis1 interaction while largely preserving physiological mitochondrial dynamics. It has demonstrated promising neuroprotective effects in multiple experimental neurological disorders[34]. However, as a peptide therapeutic, P110 remains susceptible to enzymatic degradation, rapid systemic clearance, and limited accumulation within injured brain tissue following systemic administration, substantially restricting its therapeutic efficacy[35]. Therefore, the development of an efficient delivery strategy capable of improving peptide stability, brain exposure, and therapeutic persistence represents an important prerequisite for the translational application of P110 in ICH treatment.

Although plant-derived EVs have shown promise as therapeutic carriers, their application for peptide delivery in intracerebral hemorrhage (ICH) remains largely unexplored. In particular, whether plant-derived EVs can enhance the therapeutic efficacy of mitochondria-targeted peptide interventions has not been investigated. To date, most studies have focused on delivering small molecules or nucleic acids, whereas the feasibility of using plant-derived vesicles to deliver mitochondria-targeted therapeutic peptides has received little attention. In the present study, we engineered Pn-EVs as a vesicle-based delivery platform for the systemic administration of P110 and evaluated their therapeutic potential in a collagenase-induced ICH model. The physicochemical characteristics, loading performance, release behavior, and biodistribution of Pn-EVs@P110 were investigated. Furthermore, we assessed the effects of vesicle-mediated P110 delivery on neurological outcomes, neuroinflammation, mitochondrial dynamics, and transcriptomic and metabolomic alterations following ICH. By integrating pharmaceutical characterization with mechanistic and multi-omics analyses, this study aimed to establish a plant-derived EV-based peptide delivery strategy for mitochondrial protection after ICH and to provide experimental evidence supporting the development of engineered medicinal plant vesicles as therapeutic platforms for neurological disorders.

METHODS

Animals and ICH model

Male C57BL/6 mice (6 weeks old, 20-25 g) were purchased from Jinan Pengyue Experimental Animal Center (Jinan, China). Animals were maintained under specific pathogen-free conditions at 22 ± 2 °C and 50% ± 10% relative humidity with a 12 h light/dark cycle and free access to food and water. Before experimentation, mice were allowed to acclimatize for at least 7 days.

All animal procedures were approved by the Animal Ethics Committee of Jining No. 1 People's Hospital (Approval No. JNRM-2025-DW-140), and the study followed the Animal Research: Reporting of *In Vivo* Experiments (ARRIVE) 2.0 guidelines and relevant institutional regulations.

ICH was induced using a collagenase injection model. Briefly, mice were anesthetized with sodium pentobarbital (50 mg/kg, intraperitoneal injection) and positioned in a stereotaxic frame (RWD Life Science, Shenzhen, China). Collagenase VII-S (0.05 U; MedChemExpress, Monmouth Junction, NJ, USA) was injected into the right striatum at coordinates 0.8 mm anterior, 2.0 mm lateral, and 3.5 mm ventral relative to bregma. Sham animals received an equal volume of sterile saline.

Animals were randomly assigned to Sham, ICH, ICH + P110, ICH + Pn-EVs, and ICH + Pn-EVs@P110 groups. Free P110 (40 ng/mouse), Pn-EVs (1×10^7 particles/mL), or Pn-EVs@P110 (1×10^7 particles/mL, corresponding to 33.3 ng P110/mouse based on an 80.1% association efficiency) were administered via tail vein injection (100 μL per mouse) at 0, 24, and 48 h after the first treatment. Neurological deficits were evaluated using the modified neurological severity score (mNSS) at 72 h after the first treatment. Investigators performing mNSS assessment, NeuN/terminal deoxynucleotidyl transferase dUTP nick-end labeling (TUNEL) image quantification, *In Vivo* Imaging System (IVIS) region of interest (ROI) analysis, and Western blot densitometric analysis were blinded to group allocation. Blinding was not applied during ICH model establishment, drug administration, or tissue collection.

Preparation and characterization of Pn-EVs and Pn-EVs@P110

Isolation of Pn-EVs

Fresh roots of *Panax notoginseng* were obtained from Wenshan, Yunnan Province, China. Pn-EVs were isolated by differential centrifugation followed by ultracentrifugation. Briefly, fresh roots were washed with sterile phosphate-buffered saline (PBS; Gibco, Thermo Fisher Scientific, Waltham, MA, USA) and homogenized in cold PBS. The homogenate was centrifuged at 500 × *g* for 10 min, 2,000 × *g* for 20 min, and 10,000 × *g* for 30 min to remove cell debris and large particles. The collected supernatant was then ultracentrifuged at 150,000 × *g* for 90 min using an Optima XPN-100 ultracentrifuge at 4 °C equipped with an SW41Ti rotor (Beckman Coulter, Brea, CA, USA). The pellet was washed once with PBS and subjected to a second ultracentrifugation under the same conditions. Finally, the isolated Pn-EVs were reconstituted in PBS and stored at -80 °C. Pn-EVs used in this study were prepared from at least three independent batches under standardized conditions.

Preparation of Pn-EVs@P110

P110 peptide (HY-P10368, MedChemExpress, Monmouth Junction, NJ, USA) was associated with Pn-EVs using a sonication-assisted loading strategy. Briefly, Pn-EVs (2.4×10^{10} particles/mL) were mixed with P110 (1 mg/mL) and subjected to probe sonication (40% amplitude; 45 s on/120 s off, eight cycles) in an ice bath. The suspension was subsequently incubated overnight at 4 °C to facilitate membrane recovery. Unassociated peptide was removed by ultracentrifugation at 150,000 × *g* for 60 min, and the precipitate was reconstituted in PBS to obtain Pn-EVs@P110.

Physicochemical characterization

The morphology of Pn-EVs and Pn-EVs@P110 was examined by transmission electron microscopy (TEM; Tecnai G2 Spirit BioTWIN, FEI, Hillsboro, OR, USA) after negative staining with 2% uranyl acetate. Particle size and concentration were determined using a ZetaView PMX120 nanoparticle tracking analyzer (NTA, Particle Metrix GmbH, Inning am Ammersee, Germany). All measurements were conducted in technical triplicate in accordance with the manufacturer's recommendations, and data were processed using ZetaView software.

Phytochemical profiling

The phytochemical composition of Pn-EVs was characterized using an untargeted ultra-performance liquid chromatography-high-resolution mass spectrometry (UPLC-HRMS) platform. Vesicle samples were extracted with ultrapure water containing mixed internal standards, followed by vortexing, sonication, and centrifugation. Chromatographic separation was performed on an ACQUITY UPLC HSS T3 column (100 mm × 2.1 mm, 1.8 μm) using water containing 0.1% formic acid and acetonitrile as the mobile phases. Mass spectrometric data were acquired on a Q Exactive HF mass spectrometer (Thermo Fisher Scientific, Waltham, MA, USA) operating in both positive and negative electrospray ionization modes using the Full

MS/dd-MS^2 (Top 8) acquisition method. Data processing, including peak alignment, normalization, and metabolite annotation, was performed using Progenesis QI v3.0. Putative phytochemicals were assigned by comparing their accurate mass, retention time, and MS/MS fragmentation spectra against a Traditional Chinese Medicine (TCM) database.

Drug loading, release, and storage stability

The association efficiency of P110 with Pn-EVs was measured using high-performance liquid chromatography (HPLC, Prominence Plus LC-20A; Shimadzu, Kyoto, Japan) after removal of unassociated peptide by ultracentrifugation. Association efficiency (AE) was calculated as:

$$AE\% = \frac{\text{Associated P 110}}{\text{Total P110}} \times 100\%$$

The *in vitro* release profile of P110 was evaluated using a dialysis method. Pn-EVs@P110 suspensions were placed in dialysis bags [molecular weight cut-off (MWCO) 3.5 kDa; Spectrum Laboratories, USA] in PBS (pH 7.4) at 37 °C under gentle shaking (100 rpm). At predetermined time points, aliquots were collected, and fresh medium was added. Released P110 was quantified by HPLC.

Pn-EVs and Pn-EVs@P110 were stored at 4 °C, and particle size, particle concentration, and zeta potential were periodically monitored by NTA.

In vitro experiments

Cell culture and oxygen-glucose deprivation (OGD) model

The murine microglial line BV2 and the murine hippocampal neuronal line HT22 were both purchased from Procell (Wuhan, China; CL-0493 and CL-0697, respectively). For routine propagation, the two lines were cultured in Dulbecco's Modified Eagle Medium (DMEM; Gibco, Thermo Fisher Scientific, Waltham, MA, USA) supplemented with 10% fetal bovine serum (FBS; Gibco) and 1% penicillin-streptomycin solution (Gibco) at 37 °C in a humidified incubator containing 5% CO_2. Both BV2 and HT22 cells used in the experiments were within 10 passages after recovery from cryopreservation.

For OGD induction, cells were incubated in glucose-free DMEM and transferred into a hypoxia chamber containing 1% O_2, 5% CO_2, and 94% N_2 for 6 h. Cells were returned to normoxic conditions in complete culture medium for reoxygenation. Cells were treated with free P110 (1 μM), Pn-EVs (1 × 10^7 particles/mL), or Pn-EVs@P110 (1 × 10^7 particles/mL).

Cell viability assay

Cell viability was evaluated using a Cell Counting Kit-8 (CCK-8; C0038, Beyotime Biotechnology, Shanghai, China). HT22 cells were seeded at 8 × 10^3 cells/well in 96-well plates and cultured overnight. Under normal conditions, cells were treated with P110 (1, 5, or 10 μM), Pn-EVs, or Pn-EVs@P110 (1 × 10^7, 1 × 10^8, or 1 × 10^9 particles/mL). For OGD experiments, cells underwent OGD for 6 h, followed by treatment with P110 (1 μM), Pn-EVs (1 × 10^7 particles/mL), or Pn-EVs@P110 (1 × 10^7 particles/mL) for 24 h. Three technical replicates were included for each experimental condition, and three independent biological experiments were performed. Blank wells without cells and vehicle controls were included. After the treatment period, 10 μL of CCK-8 solution was added to each well, and the plates were kept at 37 °C for 2 h, and the resulting absorbance at 450 nm was read using a Synergy2 microplate reader (BioTek, USA).

Cellular uptake

Pn-EVs@P110 were labeled with 1,1'-dioctadecyl-3,3,3',3'-tetramethylindocarbocyanine perchlorate (DiL; HY-D0083, MedChemExpress, Monmouth Junction, NJ, USA), and excess dye was removed by ultracentrifugation. Labeled vesicles were incubated with normal BV2 cells or lipopolysaccharide (LPS)-induced BV2 cells for 0.5, 3, or 6 h. Cellular uptake was subsequently examined using a confocal laser scanning microscope (FV3000, Olympus, Tokyo, Japan) following 4',6-diamidino-2-phenylindole (DAPI) (Abcam, Cambridge, UK) nuclear staining.

In vivo biodistribution and cellular localization

Pn-EVs@P110 were labeled with the near-infrared fluorescent dye 1,1'-Dioctadecyl-3,3,3',3'-tetramethylindotricarbocyanine iodide (DiR; M5122, AbMole, Houston, TX, USA), and free dye was removed by ultracentrifugation before administration. To distinguish fluorescence associated with DiR-labeled Pn-EVs@P110 from that of free DiR, ICH mice were intravenously administered free DiR or DiR-labeled Pn-EVs@P110 at an equivalent DiR dose. PBS-treated mice were used as the negative control. Whole-body fluorescence signals were acquired at 1, 4, and 12 h after injection with an IVIS Spectrum imaging system (Tanon ML500, China). The animals were then sacrificed, and the brains together with major organs were harvested and imaged *ex vivo* to evaluate tissue biodistribution.

To examine cellular localization within the injured brain, Pn-EVs@P110 were labeled with PKH67 Green Fluorescent Cell Linker Dye (HY-D1421, MedChemExpress, Monmouth Junction, NJ, USA) and intravenously administered to ICH mice. Brain sections were stained with an anti-Iba-1 antibody (Abcam, Cambridge, UK) and counterstained with DAPI. Colocalization of vesicle-associated fluorescence with microglia was analyzed using confocal laser scanning microscopy.

Neurological and histological evaluation

The mNSS was applied to grade neurological function. This composite score integrates motor, sensory, reflex, and balance/coordination items on a 0 to 18 scale, where a higher value reflects more severe neurological impairment. Cerebral edema was evaluated using the wet-dry weight method. Hematoma volume and lesion area were determined on hematoxylin and eosin (H&E; Beyotime Biotechnology, Shanghai, China)-stained brain sections and analyzed with ImageJ software (National Institutes of Health, Bethesda, MD, USA).

For histological quantification, three independent mice were analyzed in each group ($n = 3$). Coronal brain sections encompassing the hematoma were selected, and NeuN-positive neurons and TUNEL-positive cells were quantified in the perihematomal regions using multiple non-overlapping microscopic fields. The same sampling and quantification criteria were applied across all experimental groups. Neuronal survival was evaluated by immunofluorescence staining for NeuN (Synaptic Systems, Göttingen, Germany). Apoptotic cell death in perihematomal brain tissue was detected with a TUNEL assay kit (Abcam, Cambridge, UK), following the protocol supplied by the manufacturer.

Transcriptomic and metabolomic analyses

Transcriptomic analysis

Perihematomal brain tissues were collected from the indicated experimental groups for transcriptomic analysis. Total RNA was isolated with TRIzol reagent (Invitrogen, Carlsbad, CA, USA). Sequencing libraries were constructed following standard protocols and run on an Illumina NovaSeq 6000 platform (Illumina, San Diego, CA, USA). After low-quality reads were removed during quality filtering, the resulting clean reads were mapped to the Mus musculus reference genome using HISAT2, and transcript abundance was

estimated through routine bioinformatics workflows. Differentially expressed genes (DEGs) were identified using DESeq2 with thresholds of $P < 0.05$ and $|\log_2 \text{fold change}| > 1$. Principal component analysis (PCA), Gene Ontology (GO), and Kyoto Encyclopedia of Genes and Genomes (KEGG) enrichment analyses were performed using ClusterProfiler (v4.6.0) and Metascape.

Metabolomic analysis

Untargeted metabolomic profiling was conducted on perihematomal brain tissues using an ultra-high-performance liquid chromatography (UHPLC)-Q Exactive Plus Orbitrap mass spectrometry platform (Thermo Fisher Scientific, Waltham, MA, USA). The acquired LC-MS files were first reformatted in ProteoWizard (v3.0.8789), after which XCMS (v3.12.0) handled peak picking, retention time correction, peak area integration, and relative quantitation. Metabolites were annotated by matching accurate mass, retention time, MS/MS fragmentation spectra, and collision cross-section (CCS) values against an in-house spectral library and public databases, including HMDB, METLIN, MassBank, and mzCloud. Confidence of identification was graded following the Metabolomics Standards Initiative (MSI) framework, and only metabolites with an identification confidence of Level 2 or above were retained for downstream analyses. Data preprocessing included filtering, normalization, and missing-value imputation prior to quality assessment. PCA, orthogonal partial least squares discriminant analysis (OPLS-DA), differential metabolite analysis, and KEGG pathway enrichment were subsequently performed. Differential metabolites were defined as metabolites with $P < 0.05$ and $|\log_2 \text{fold change}| > 1$.

Evaluation of neuroinflammation and oxidative stress

Quantitative real-time PCR (qRT-PCR)

Total RNA was extracted from perihematomal brain tissue or BV2 cells using TRIzol reagent (Invitrogen, Carlsbad, CA, USA) and reverse-transcribed into complementary DNA (cDNA) with a commercial kit. Amplification and fluorescence detection were run on a QuantStudio real-time PCR system with SYBR Green Master Mix (both from Applied Biosystems, Foster City, CA, USA). The relative expression of each target gene was computed by the 2-ΔΔCt method, normalizing Ct values to β-actin as the endogenous reference. All primer sequences are provided in Supplementary Table 1.

Immunohistochemical and fluorescence analyses

Paraffin-embedded or frozen brain sections underwent immunohistochemical or immunofluorescence staining following standard protocols. Following antigen retrieval and blocking of nonspecific binding, the sections were exposed overnight at 4 °C to a primary antibody raised against the microglial marker Iba-1 (Abcam, Cambridge, UK), followed by an appropriate horseradish peroxidase (HRP)-conjugated or fluorophore-conjugated secondary antibody. For ROS detection, brain sections were stained with dihydroethidium (DHE; Abcam) according to the manufacturer's instructions. Cell nuclei were counterstained with hematoxylin or DAPI as appropriate. Representative images were acquired using a Pannoramic MIDI II scanner (3DHISTECH, Budapest, Hungary) or a confocal laser scanning microscope (Olympus FV3000, Tokyo, Japan). Quantitative image analysis, including Iba-1 immunoreactivity, microglial morphology (Sholl analysis), and DHE fluorescence intensity, was performed using ImageJ software.

Oxidative DNA damage was quantified using an 8-hydroxy-2'-deoxyguanosine (8-OHdG) enzyme-linked immunosorbent assay (ELISA) kit (E-EL-0028, Elabscience Biotechnology, Wuhan, China).

Assessment of mitochondrial morphology and function

Immunofluorescence staining

Immunofluorescence staining was performed to evaluate mitochondrial morphology and microglial mitochondrial dynamics in brain tissues and cultured cells. Samples were incubated with the indicated

primary antibodies overnight at 4 °C, followed by fluorophore-conjugated secondary antibodies. DAPI was used to counterstain cell nuclei. An Olympus FV3000 confocal laser scanning microscope (Olympus, Tokyo, Japan) was used to acquire the fluorescence images, while ImageJ software was used to quantify fluorescence intensity and colocalization. Brain sections were stained with antibodies against Iba-1 and TOM20.

Confocal microscopy was used to evaluate mitochondrial morphology within microglia.

Western blot analysis

Perihematomal brain tissue was lysed in radioimmunoprecipitation assay (RIPA) buffer containing protease and phosphatase inhibitors. Equivalent protein loads were resolved by sodium dodecyl sulfate-polyacrylamide gel electrophoresis (SDS-PAGE) and blotted onto polyvinylidene fluoride (PVDF) membranes. Membranes were incubated overnight at 4 °C with primary antibodies against mitochondrial dynamics-related proteins, including Drp1, phospho-Drp1 (Ser616), MFN2, and OPA1, followed by HRP-conjugated secondary antibodies. Protein bands were visualized using enhanced chemiluminescence reagents and quantified with ImageJ software after normalization to β-actin.

Detailed information on primary and secondary antibodies used in this study is summarized in Supplementary Table 2.

Ultrastructural and functional assessment of mitochondria in BV2 cells

LPS-stimulated BV2 cells were used to evaluate mitochondrial morphology and function. Mitochondrial ultrastructure was examined by TEM. For ultrastructural examination, the cells were immobilized in 2.5% glutaraldehyde and post-fixed with osmium tetroxide. After dehydration, the specimens were embedded in epoxy resin, and the polymerized blocks were cut into ultrathin sections. These sections received uranyl acetate and lead citrate staining in turn and were then observed with a TEM. Mitochondrial morphology was quantified by measuring mitochondrial area and aspect ratio using ImageJ software. Intracellular ATP levels were determined using a commercial ATP assay kit (S0026, Beyotime Biotechnology, Shanghai, China), and mitochondrial membrane potential was assessed using a JC-1 Mitochondrial Membrane Potential Assay Kit (C2006, Beyotime Biotechnology, Shanghai, China). The JC-1 red/green fluorescence ratio was quantified using ImageJ software.

Statistical analysis

Each experiment included at least three independent biological replicates unless specified otherwise. Results are expressed as mean ± standard deviation (SD). Statistical analyses were performed using GraphPad Prism 9.0 (GraphPad Software, San Diego, CA, USA). Comparisons between two groups were conducted using an unpaired two-tailed Student's *t*-test, while multiple-group comparisons were analyzed by one-way analysis of variance (ANOVA) followed by Tukey's post hoc test. Statistical significance was defined as $P < 0.05$.

RESULTS

Characterization of Pn-EVs and Pn-EVs@P110

To prepare a plant-derived vesicle-based delivery system for subsequent biological evaluation, Pn-EVs were first isolated from *Panax notoginseng* roots and associated with P110 by a sonication-assisted strategy [Figure 1A]. The purified Pn-EVs exhibited the classic cup-shaped morphology of EVs under TEM [Figure 1B]. UPLC-HRMS analysis detected multiple representative *Panax notoginseng*-derived ginsenosides in the purified Pn-EVs, including ginsenoside Rg1, ginsenoside F5, gypenoside XVII, and ginsenoside Rb1 [Figure 1C]. Representative LC-MS/MS spectral matching further supported the identification of ginsenoside Rg1 [Figure 1D].

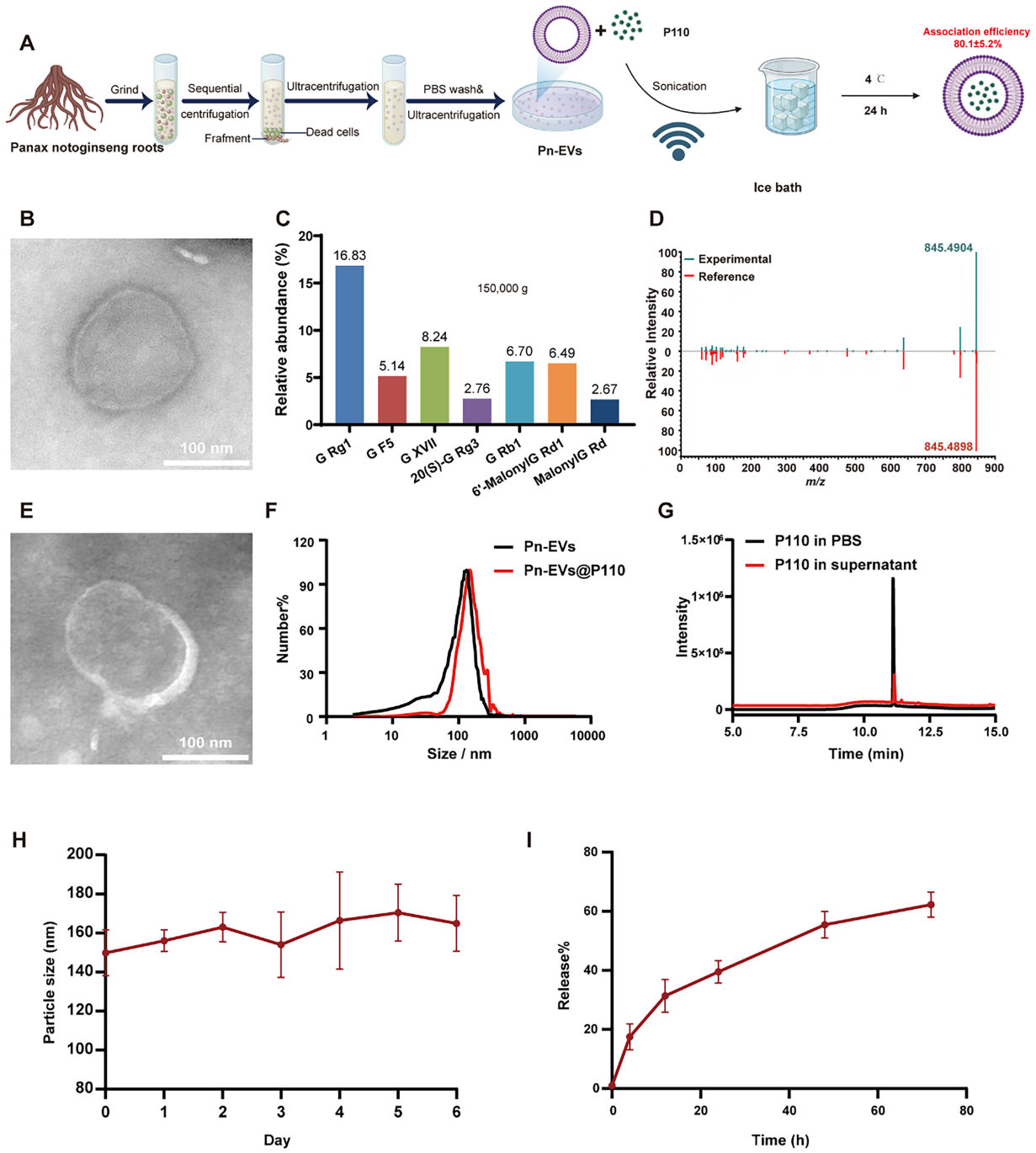


Figure 1. Preparation and characterization of Pn-EVs@P110. (A) Schematic illustration of Pn-EV isolation and Pn-EVs@P110 preparation; (B) Representative TEM image of Pn-EVs; (C) Relative abundance of representative ginsenosides detected in Pn-EVs; (D) Representative LC-MS/MS identification of ginsenoside Rg1; (E) Representative TEM image of Pn-EVs@P110; (F) Particle-size distributions of Pn-EVs and Pn-EVs@P110 measured by NTA; (G) HPLC chromatograms of P110 in PBS and P110 in the supernatant after the association procedure; (H) Particle-size stability of Pn-EVs@P110 during storage at 4 °C for 6 days; (I) *In vitro* release of P110 from Pn-EVs@P110 over 72 h. Data are presented as mean ± SD. The schematic in Figure 1A was adapted and modified from our previously published work[15]. Pn-EVs: *Panax notoginseng*-derived extracellular vesicle-like nanovesicles; TEM: transmission electron microscopy; LC-MS/MS: liquid chromatography-tandem mass spectrometry; NTA: nanoparticle tracking analysis; HPLC: high-performance liquid chromatography; PBS: phosphate-buffered saline; SD: standard deviation.

Following P110 loading, Pn-EVs@P110 retained their structural integrity without obvious aggregation [Figure 1E]. NTA analysis showed a narrow particle size distribution centered at approximately 150 nm, with a slight increase after P110 loading [Figure 1F]. HPLC analysis demonstrated an association efficiency of

80.1% ± 5.2% [Figure 1G]. Furthermore, Pn-EVs@P110 maintained a relatively stable particle size during storage at 4 °C for 6 days, with minimal change [Figure 1H]. Pn-EVs@P110 showed a prolonged *in vitro* release pattern, reaching roughly 60% of the loaded drug over 72 h [Figure 1I]. These results confirmed the successful preparation and physicochemical characterization of Pn-EVs@P110 for subsequent experiments.

Pn-EVs@P110 exhibited enhanced brain accumulation and microglial uptake after systemic administration.

Following the physicochemical characterization of Pn-EVs@P110, we next evaluated its biodistribution and cellular uptake after systemic administration. To distinguish fluorescence associated with DiR-labeled Pn-EVs@P110 from that of free DiR, ICH mice were intravenously administered free DiR or DiR-labeled Pn-EVs@P110. Whole-body fluorescence imaging demonstrated progressive accumulation of vesicle-associated signals within the cranial region from 1 to 12 h after injection, whereas free DiR produced substantially weaker fluorescence signals in the cranial region [Figure 2A and B]. *Ex vivo* imaging further confirmed detectable fluorescence signals in the brain, in addition to distribution in the liver and spleen [Figure 2C and D]. In contrast, free DiR showed the most fluorescence signals in peripheral organs, particularly the heart, liver, and kidney [Figure 2C and D].

Confocal imaging of perihematomal brain sections revealed substantial colocalization between vesicle-associated fluorescence and Iba-1-positive microglia [Figure 2E], indicating cellular uptake within inflammatory regions. *In vitro* studies demonstrated time-dependent cellular uptake of Dil-labeled Pn-EVs@P110 by BV2 cells [Figure 2F]. Quantitative analysis of intracellular Dil fluorescence intensity confirmed a progressive increase in fluorescence from 0.5 to 6 h in both control and LPS-stimulated BV2 cells [Figure 2G]. The LPS-stimulated group showed higher fluorescence than the control group at 3 h, whereas no significant difference was observed between groups at 0.5 or 6 h. These results confirmed that intravenously administered Pn-EVs@P110 accumulated efficiently in the injured brain and were readily internalized by microglial cells.

Pn-EVs@P110 improved neurological outcomes and reduced brain injury after ICH

Following confirmation of brain accumulation and microglial uptake, we next evaluated the *in vivo* efficacy of Pn-EVs@P110. The therapeutic efficacy of Pn-EVs@P110 was evaluated using a collagenase-induced ICH model, with mNSS assessed at 72 h after the first treatment [Figure 3A]. Compared with untreated ICH mice, administration of Pn-EVs@P110 significantly reduced hematoma volume and brain water content and improved neurological function, as indicated by reduced mNSS [Figure 3B-D].

Histological examination revealed severe neuronal degeneration and tissue disorganization in perihematomal regions following ICH. These pathological changes were partially alleviated by P110 or Pn-EVs alone and were further improved in the Pn-EVs@P110 group [Figure 3E and F]. NeuN immunostaining demonstrated increased neuronal survival following treatment [Figure 3G and H], whereas TUNEL staining revealed a significant reduction in apoptotic cells [Supplementary Figure 1].

To further evaluate the cytocompatibility and neuroprotective effect of Pn-EVs@P110 *in vitro*, CCK-8 assays further demonstrated that Pn-EVs and Pn-EVs@P110 exhibited no detectable cytotoxicity at the tested concentrations and significantly improved HT22 cell viability following oxygen-glucose deprivation injury [Supplementary Figure 2]. Notably, free P110 treatment showed limited improvement under identical dosing conditions, highlighting the advantage of vesicle-mediated delivery. These results demonstrated the therapeutic efficacy of Pn-EVs@P110 against ICH-associated brain injury and supported its subsequent mechanistic investigation.

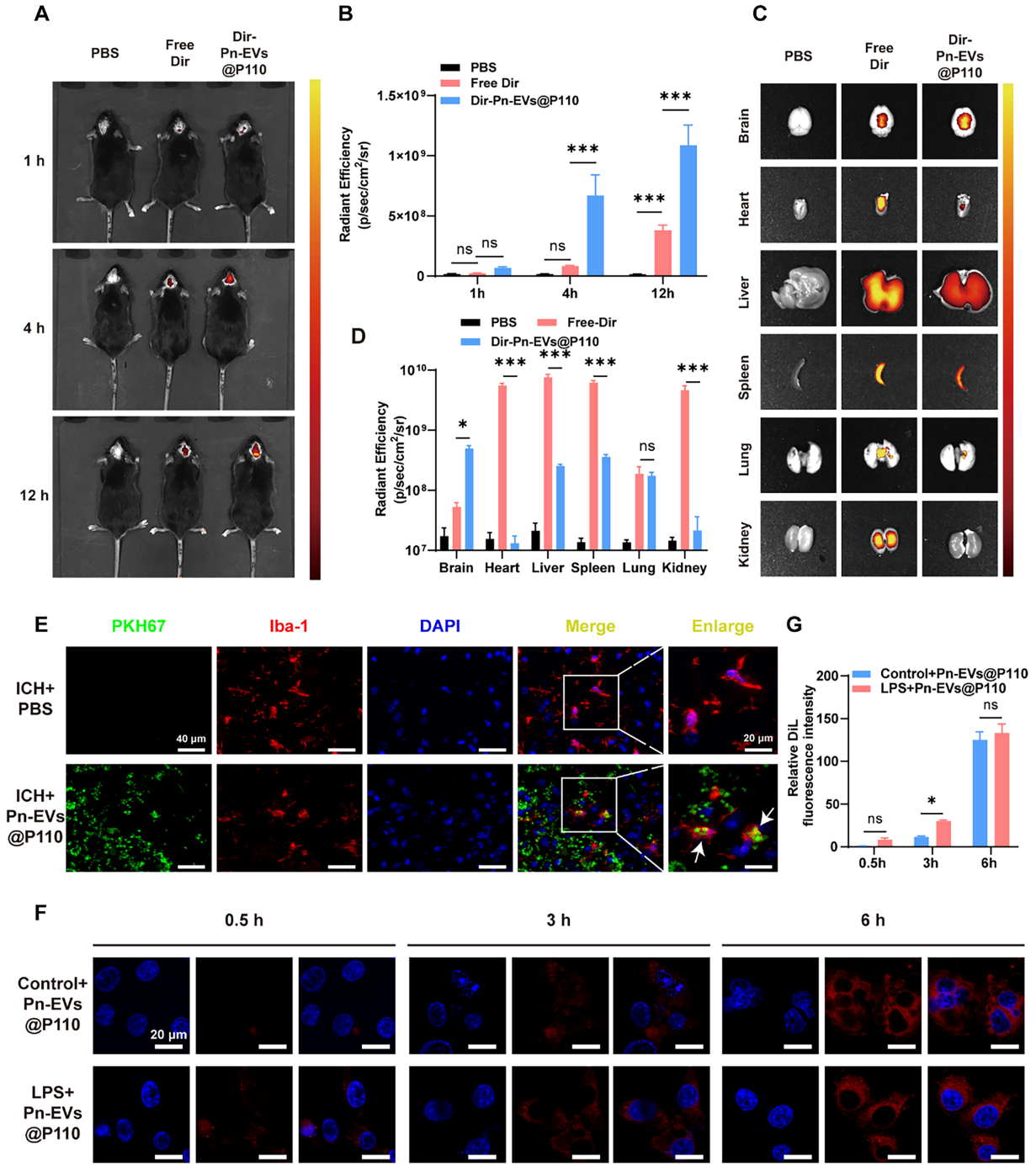


Figure 2. Biodistribution and microglial uptake of Pn-EVs@P110. (A) Representative *in vivo* IVIS images of mice following intravenous administration of PBS, free DiR, or DiR-labeled Pn-EVs@P110 at 1, 4, and 12 h; (B) Quantification of brain radiant efficiency at the indicated time points; (C) Representative *ex vivo* IVIS images of major organs (brain, heart, liver, spleen, lung, kidney); (D) Quantification of radiant efficiency in each organ; (E) Representative confocal images of perihematomal brain sections showing PKH67-labeled Pn-EVs@P110 (green) colocalized with Iba-1+ microglia (red) and DAPI (blue). Right panels show enlarged views; arrows indicate colocalization; (F) Representative confocal images showing time-dependent uptake of labeled Pn-EVs@P110 by BV2 microglia under control or LPS stimulation (0.5, 3, and 6 h); (G) Quantification of relative intracellular DiI fluorescence intensity at the indicated time points. Data are presented as mean ± SD. For (A-E), $n = 3$ mice/group; for (F and G), data were obtained from three independent biological experiments ($n = 3$). Statistical comparisons are indicated by the brackets; $^{*}P < 0.05$, $^{***}P < 0.001$. Pn-EVs: *Panax notoginseng*-derived extracellular vesicle-like nanovesicles; IVIS: *in vivo* imaging system; PBS: phosphate-buffered saline; DiR: 1,1′-dioctadecyl-3,3,3′,3′-tetramethylindotricarbocyanine iodide; DAPI: 4′,6-diamidino-2-phenylindole; Iba-1: ionized calcium-binding adapter molecule 1; LPS: lipopolysaccharide; DiI: 1,1′-dioctadecyl-3,3,3′,3′-tetramethylindocarbocyanine perchlorate; SD: standard deviation; PKH67: PKH67 Green Fluorescent Cell Linker Dye; ns: not significant.

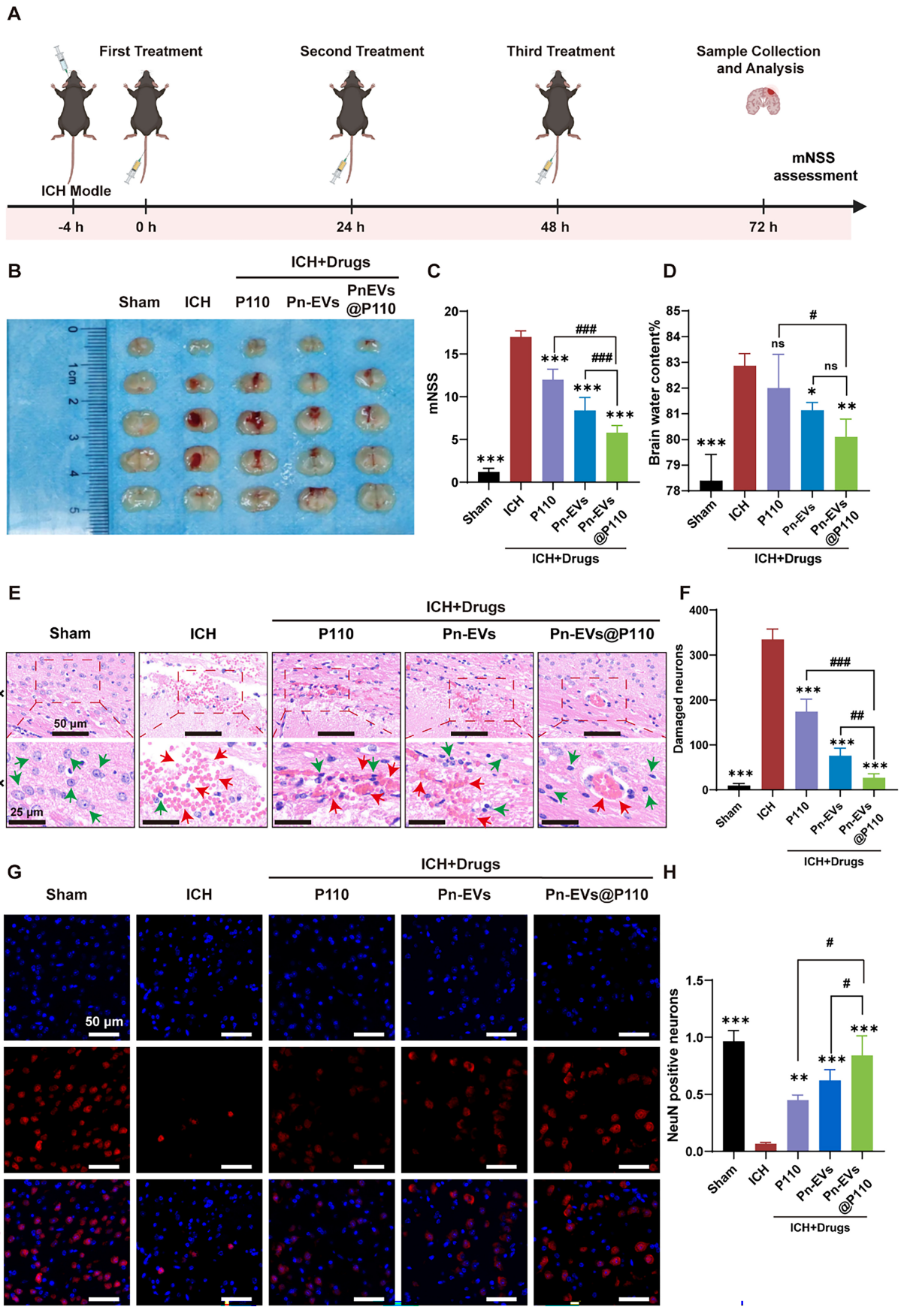


Figure 3. Pn-EVs@P110 improves neurological outcomes and reduces brain injury after the first treatment (*in vivo*). (A) Experimental timeline for collagenase-induced ICH model establishment, drug administration, mNSS assessment, and sample collection. Created in BioRender. Chen, B. (2026) https://BioRender.com/67tdrxr; (B) Representative whole-brain images showing hematoma in 5 groups; (C) mNSS; (D) brain water content in each group; (E) Representative H&E staining of perihematomal brain sections (20× and 40×). Arrowheads indicate injured (red)/degenerating (green) neurons and tissue damage; (F) Quantification of damaged neurons in

perihematomal regions; (G) Representative immunofluorescence images of NeuN (red) and DAPI (blue) in perihematomal regions; (H) Quantification of NeuN-positive neurons. Data are presented as mean ± SD; $n = 3$ mice/group. $^{*}P < 0.05$, $^{**}P < 0.01$, $^{***}P < 0.001$ *vs.* ICH; $^{\#}P < 0.05$, $^{\#\#}P < 0.01$, $^{\#\#\#}P < 0.001$ *vs.* Pn-EVs or P110 as indicated by the brackets. ICH: Intracerebral hemorrhage; mNSS: modified neurological severity score; H&E: hematoxylin and eosin; NeuN: neuronal nuclei; DAPI: 4′,6-diamidino-2-phenylindole; Pn-EVs: *Panax notoginseng*-derived extracellular vesicle-like nanovesicles; SD: standard deviation; ns: not significant.

Transcriptomic and metabolomic analyses revealed modulation of inflammation- and mitochondrial-related pathways

To further investigate the molecular changes associated with the therapeutic effects of Pn-EVs@P110, transcriptomic and metabolomic analyses were performed using perihematomal brain tissues. PCA demonstrated distinct clustering among the ICH, Pn-EVs, and Pn-EVs@P110 groups [Figure 4A]. Differential gene expression analysis showed that Pn-EVs@P110 reversed a substantial proportion of ICH-associated transcriptional changes [Figure 4B]. Representative mitochondria-associated genes, including ATP8, Tufm, and Tomm40l, were partially restored after Pn-EVs@P110 treatment [Figure 4C]. KEGG enrichment revealed that the DEGs were concentrated in terms governing inflammatory and immune responses, with the TNF signaling pathway, cytokine-cytokine receptor interaction, and chemokine signaling pathway ranking among the most enriched [Figure 4D]. Gene set enrichment analysis further demonstrated suppression of the innate immune response and enrichment of a mitochondrial ATP synthesis-related gene set following Pn-EVs@P110 treatment [Figure 4E and F].

Metabolomic profiling was subsequently performed to evaluate treatment-associated metabolic alterations. Differential metabolite analysis revealed both shared and treatment-specific metabolic changes among the comparison groups [Figure 4G and H]. KEGG enrichment analysis demonstrated that the altered metabolites were mainly associated with energy metabolism, oxidative phosphorylation, lipid metabolism, and other metabolic processes [Figure 4I]. These transcriptomic and metabolomic findings provided complementary molecular evidence of coordinated changes in inflammatory signaling and mitochondrial-related metabolic processes, supporting further evaluation of neuroinflammation and mitochondrial function.

Pn-EVs@P110 attenuated microglial activation and inflammatory responses after ICH

Based on the transcriptomic findings implicating inflammatory pathways, we next evaluated microglial activation and inflammatory responses in perihematomal brain tissues. Immunohistochemical and immunofluorescence analyses demonstrated substantial microglial activation in perihematomal regions following ICH, characterized by increased Iba-1-positive cell density and morphological transformation toward an activated phenotype [Figure 5A and B]. Treatment with Pn-EVs@P110 significantly reduced microglial activation compared with untreated ICH mice and mice receiving either P110 or Pn-EVs alone [Figure 5A and B]. Sholl analysis demonstrated increased process complexity and restoration of ramified microglial morphology following Pn-EVs@P110 treatment [Figure 5C and D]. qRT-PCR confirmed that the perihematomal tissue expressed markedly lower levels of the pro-inflammatory cytokines IL-1β, IL-6, and TNF-α [Figure 5E]. Furthermore, DHE staining demonstrated reduced ROS generation, while 8-OHdG quantification showed attenuation of oxidative DNA damage after treatment [Figure 5F-H]. These results demonstrated that Pn-EVs@P110 effectively attenuated microglial activation, neuroinflammation, and oxidative stress following ICH.

Pn-EVs@P110 improved mitochondrial dynamics and mitochondrial function

Given the attenuation of neuroinflammation and oxidative stress, we next evaluated whether Pn-EVs@P110 restored mitochondrial dynamics and function. Western blot analysis showed that ICH induced significant upregulation of Drp1 and phosphorylated Drp1 (Ser616), accompanied by reduced expression of mitochondrial fusion proteins MFN2 and OPA1 [Figure 6A-H]. Pn-EVs@P110 treatment significantly attenuated these alterations and partially restored the balance between mitochondrial fission and fusion [Figure 6A-H].

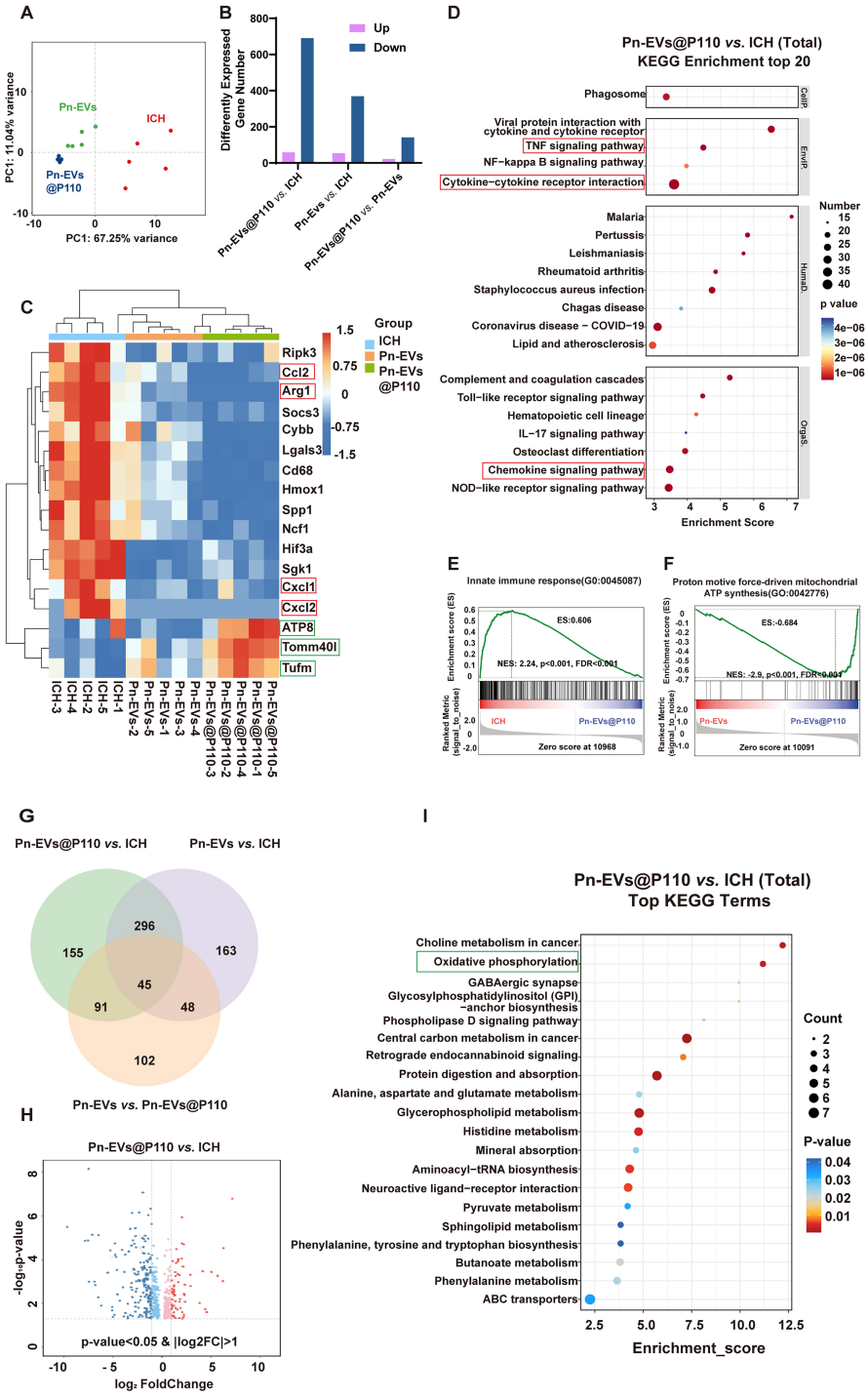


Figure 4. Transcriptomic and metabolomic analyses reveal suppression of inflammatory signaling and modulation of mitochondrial-related pathways after Pn-EVs@P110 treatment (*in vivo*, perihematomal tissue). (A) PCA score plot showing global transcriptional differences among groups; (B) Number of DEGs in pairwise comparisons; (C) Heatmap of representative inflammation-related and mitochondria-associated genes across groups; (D) KEGG enrichment analysis of total DEGs in Pn-EVs@P110 *vs.* ICH (top 20 terms); (E and F) GSEA showing representative enrichment of innate immune response and mitochondrial ATP synthesis-related gene sets; (G) Venn diagram showing overlap of differential metabolites among comparisons; (H) Volcano plot of differential metabolites ($P < 0.05$ and $|\log_2$ fold change $|> 1$, as indicated); (I) Top KEGG terms enriched in Pn-EVs@P110 *vs.* ICH. $n = 4$ independent biological samples/group. PCA: Principal component analysis; DEGs: differentially expressed genes; KEGG: Kyoto Encyclopedia of Genes and Genomes; GSEA: gene set enrichment analysis; ATP: adenosine triphosphate; Pn-EVs: *Panax notoginseng*-derived extracellular vesicle-like nanovesicles; ICH: intracerebral hemorrhage.

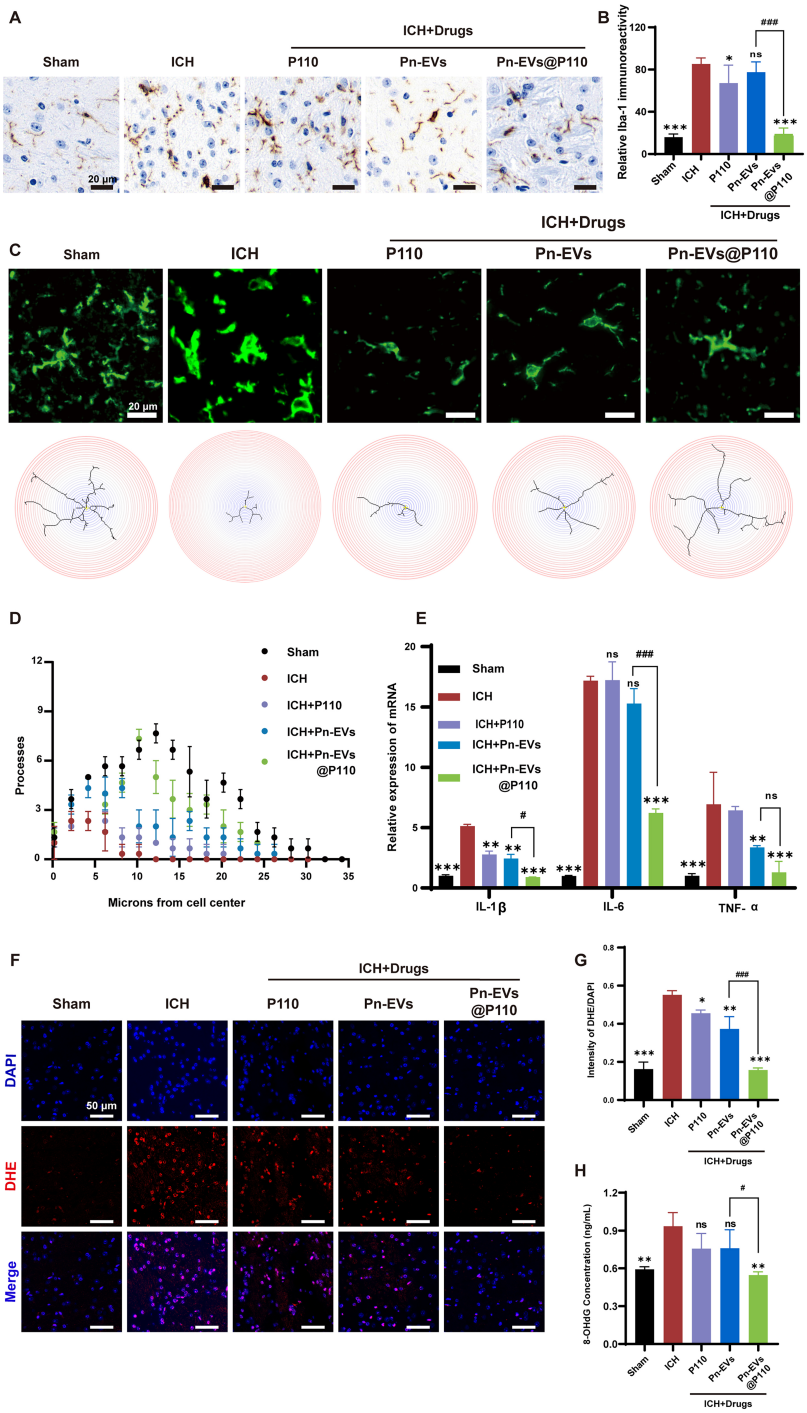


Figure 5. Pn-EVs@P110 suppresses microglial activation, neuroinflammation, and oxidative stress (*in vivo*). (A) Representative Iba-1 immunohistochemistry images in perihematomal regions; (B) Quantification of relative Iba-1 immunoreactivity; (C) Representative immunofluorescence images of activated microglia (Iba-1, green) and corresponding Sholl reconstruction maps; (D) Sholl analysis quantifying microglial process complexity; (E) qRT-PCR analysis of pro-inflammatory cytokine mRNA levels (IL-1β, IL-6, TNF-α) in perihematomal tissue; (F) Representative DHE staining images (red) with DAPI (blue); (G) Quantification of DHE fluorescence intensity; (H) 8-OHdG concentration as a marker of oxidative DNA damage. Data are presented as mean ± SD; $n = 3$ mice/group. $^{*}P < 0.05$, $^{**}P < 0.01$, $^{***}P < 0.001$ *vs.* ICH; $^{\#}P < 0.05$, $^{\#\#}P < 0.01$, $^{\#\#\#}P < 0.001$ *vs.* Pn-EVs or P110, as indicated by the brackets. Iba-1: Ionized calcium-binding adapter molecule 1; qRT-PCR: quantitative real-time polymerase chain reaction; mRNA: messenger RNA; IL-1β: interleukin-1β; IL-6: interleukin-6; TNF-α: tumor necrosis factor-α; DHE: dihydroethidium; DAPI: 4′,6-diamidino-2-phenylindole; 8-OHdG: 8-hydroxy-2′-deoxyguanosine; Pn-EVs: *Panax notoginseng*-derived extracellular vesicle-like nanovesicles; ICH: intracerebral hemorrhage; SD: standard deviation; ns: not significant.

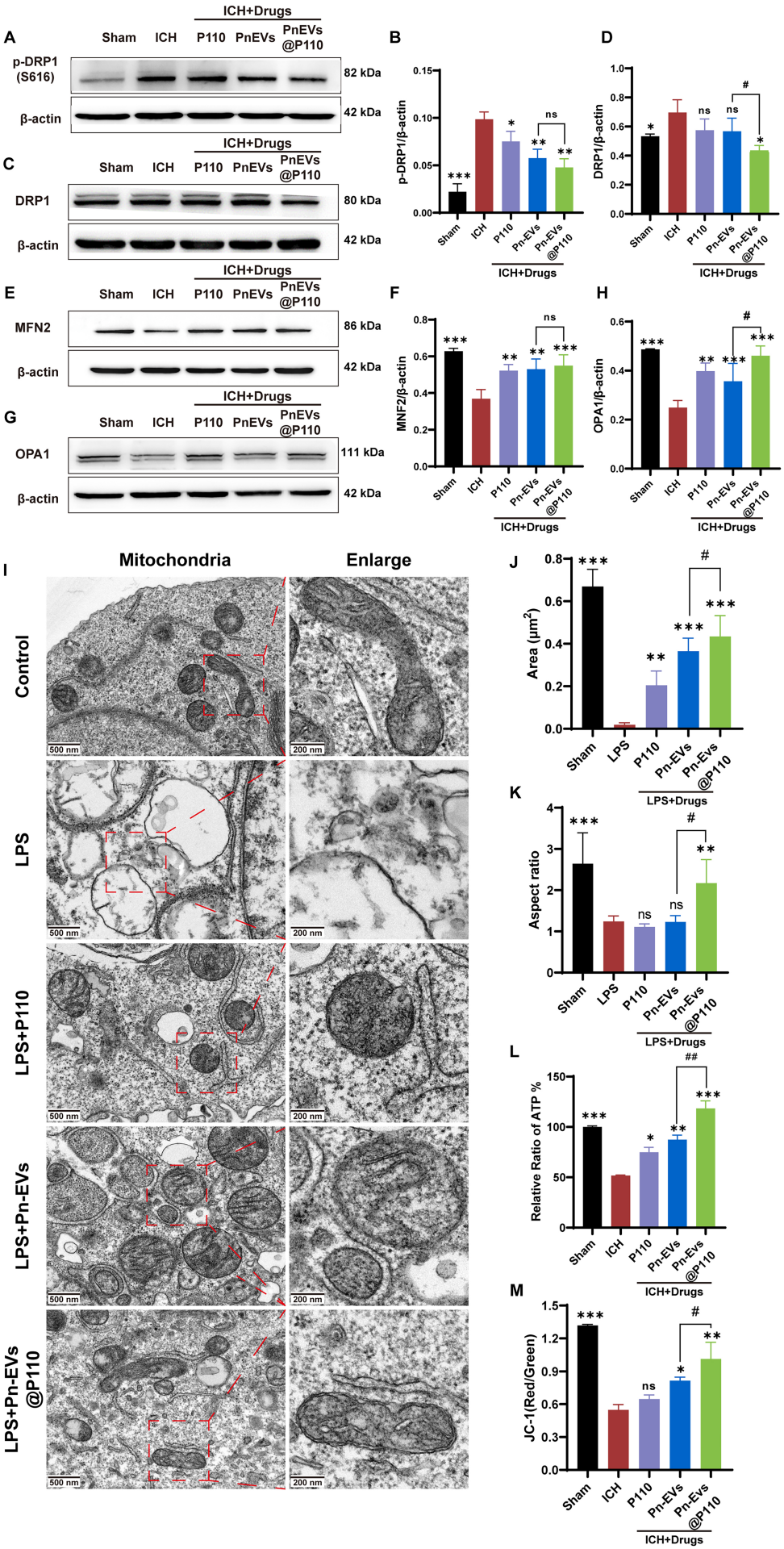

A
ICH+Drugs
Sham
ICH
P110
PnEVs
PnEVs @P110
p-DRP1 (S616)
82 kDa
β-actin
42 kDa
B
p-DRP1/β-actin
D
DRP1/β-actin
C
DRP1
80 kDa
E
MFN2
86 kDa
F
MNF2/β-actin
H
OPA1/β-actin
G
OPA1
111 kDa
I
Mitochondria
Enlarge
Control
LPS
LPS+P110
LPS+Pn-EVs
LPS+Pn-EVs @P110
500 nm
200 nm
J
Area (μm²)
LPS+Drugs
K
Aspect ratio
L
Relative Ratio of ATP %
M
JC-1(Red/Green)

Figure 6. Pn-EVs@P110 restores mitochondrial dynamics and function by inhibiting excessive fission (*in vivo* and *in vitro*). (A, C, E, and G) Representative Western blots of mitochondrial fission/fusion-related proteins in perihematomal tissue, including p-Drp1 (S616), Drp1, MFN2, and OPA1 (β-actin as loading control); (B, D, F, and H) Densitometric quantification of corresponding protein levels normalized to β-actin; (I) Representative TEM images of mitochondria in BV2 cells under control or LPS stimulation with indicated treatments (P110, Pn-EVs, Pn-EVs@P110). Boxes indicate regions shown at higher magnification; (J and K) Quantification of mitochondrial morphology parameters (area and aspect ratio) based on TEM images; (L) Intracellular ATP levels in BV2 cells under indicated conditions; (M) Mitochondrial membrane potential assessed by JC-1 red/green ratio. Data are presented as mean ± SD. For (A-H), $n = 3$ mice/group; for I-M, data were obtained from three independent biological experiments ($n = 3$). $^{*}P < 0.05$, $^{**}P < 0.01$, $^{***}P < 0.001$ *vs*. ICH (or LPS, as appropriate); $^{\#}P < 0.05$, $^{\#\#}P < 0.01$, $^{\#\#\#}P < 0.001$ *vs*. Pn-EVs or P110 as indicated by the brackets. p-Drp1: Phosphorylated dynamin-related protein 1; Drp1: dynamin-related protein 1; MFN2: mitofusin 2; OPA1: optic atrophy 1; TEM: transmission electron microscopy; LPS: lipopolysaccharide; ATP: adenosine triphosphate; JC-1: 5,5′,6,6′-tetrachloro-1,1′,3,3′-tetraethylbenzimidazolylcarbocyanine iodide; Pn-EVs: *Panax notoginseng*-derived extracellular vesicle-like nanovesicles; ICH: intracerebral hemorrhage; SD: standard deviation; ns: not significant.

TEM images of LPS-stimulated BV2 cells further demonstrated improved mitochondrial morphology following treatment. *In vitro* studies using LPS-stimulated BV2 cells revealed severe mitochondrial fragmentation and swelling after LPS induction. In contrast, Pn-EVs@P110 treatment markedly preserved mitochondrial ultrastructure and maintained more intact cristae [Figure 6I]. Consistently, immunofluorescence staining showed increased TOM20 immunoreactivity accompanied by reduced Iba-1 immunoreactivity in the perihematomal region following Pn-EVs@P110 treatment [Supplementary Figure 3]. Quantitative analysis further demonstrated significant increases in mitochondrial area and aspect ratio following Pn-EVs@P110 treatment [Figure 6J and K]. Consistent with these morphological observations, Pn-EVs@P110 significantly improved mitochondrial membrane potential and intracellular ATP production compared with untreated cells [Figure 6L and M]. These results demonstrated that Pn-EVs@P110 improved mitochondrial dynamics and mitochondrial function following inflammatory stimulation.

DISCUSSION

Our findings show that incorporating P110 into *Panax notoginseng*-derived extracellular vesicle-like nanovesicles substantially improved its therapeutic efficacy in experimental ICH. Although free P110 has previously shown neuroprotective potential by modulating mitochondrial dynamics, its therapeutic application is limited by poor stability and limited tissue exposure. In the current study, Pn-EVs-mediated delivery significantly enhanced the overall therapeutic response, as reflected by improved neurological outcomes, reduced hematoma volume, attenuated cerebral edema, and decreased neuronal injury. These findings suggest that the therapeutic limitations of peptide-based mitochondrial modulators may be partially overcome through vesicle-mediated delivery strategies. More importantly, the present findings demonstrate the feasibility of using engineered plant-derived EVs as peptide delivery platforms for neurological disorders, thereby extending the potential applications of medicinal plant vesicles beyond their intrinsic biological activities. Recent studies have similarly highlighted the potential of engineered plant-derived EVs as therapeutic and targeted delivery platforms[9,10].

The greater efficacy of Pn-EVs@P110 may be related to improved P110 delivery. A notable finding was the increased accumulation of vesicle-associated signals within perihematomal regions following systemic administration. Previous studies have suggested that disruption of the blood-brain barrier after ICH may facilitate nanoparticle penetration into injured brain tissue. Under these pathological conditions, Pn-EVs may function as protective carriers that prolong peptide availability and increase local exposure at sites of injury. In addition, the sustained release profile observed *in vitro* may further extend therapeutic activity. Although the precise pharmacokinetic behavior of P110 was not evaluated in the present study, the superior therapeutic efficacy of Pn-EVs@P110 compared with free P110 supports the importance of delivery optimization for peptide-based therapeutics. Compared with synthetic nanocarriers, plant-derived EVs additionally offer favorable biocompatibility, scalable production, and the potential to carry endogenous bioactive cargos, making them attractive candidates for therapeutic delivery[9,10,12].

Beyond improving delivery, Pn-EVs@P110 treatment was associated with modulation of multiple pathological processes involved in secondary brain injury. Mitochondrial dysfunction is increasingly recognized as a central mechanism linking oxidative stress, inflammatory activation, and neuronal damage following ICH[29,30,36]. Consistent with the known biological activity of P110, treatment reduced microglial activation, attenuated oxidative stress, and partially restored mitochondrial morphology and function. Furthermore, transcriptomic and metabolomic analyses revealed coordinated regulation of inflammation-related pathways and mitochondrial energy metabolism. These molecular alterations were further supported by reduced expression of pro-inflammatory cytokines, restoration of mitochondrial dynamics-related protein expression, and improved mitochondrial ultrastructure and bioenergetic function, providing complementary evidence across multi-omics, histological, and functional analyses. Together, these findings support the concept that restoration of mitochondrial homeostasis contributes to the observed neuroprotective effects. Recent studies have also highlighted the potential of EVs to modulate mitochondrial biology and deliver mitochondria-associated therapeutic components[37,38]. Nevertheless, the current omics analyses remain associative and do not directly measure mitochondrial respiration; additional studies employing genetic or pharmacological manipulation of mitochondrial dynamics will be required to establish direct causal mechanisms.

An additional finding of interest is the potential therapeutic relevance of plant-derived EVs themselves. Pn-EVs alone produced moderate protective effects in several experimental outcomes, suggesting that vesicle-associated endogenous cargos may contribute to biological activity. Because *Panax notoginseng* contains numerous bioactive constituents with anti-inflammatory and antioxidant properties, some of these components may be retained within vesicles and contribute to the overall therapeutic response. This observation raises the possibility that plant-derived EVs may function not only as delivery vehicles but also as biologically active therapeutic platforms. Further phytochemical and lipidomic characterization will be important for defining the molecular composition of Pn-EVs and clarifying the contribution of endogenous cargo to their biological effects.

Limitations

Several limitations should be acknowledged. First, although differential ultracentrifugation enabled efficient isolation of Pn-EVs, additional purification and molecular characterization are needed to establish standardized quality-control criteria for plant-derived EVs. Although TET8/TET7 and PEN1/SYP121 have been proposed as candidate plant EV-associated markers, validated marker panels for specific plant-derived vesicles remain limited. The present TEM and NTA analyses do not provide a quantitative purity index or determine the proportion of intact plant-derived EVs within the total nanoparticle population. A previous study of *Panax notoginseng*-derived extracellular vesicle-like nanovesicles similarly did not experimentally verify these candidate protein markers[21]. In the present study, Pn-EVs characterization was supported by complementary TEM, NTA, UPLC-HRMS, and MS/MS-based evidence. Second, the behavioral assessment was focused on acute neurological deficits at 72 h after the first treatment and did not comprehensively evaluate cognitive, affective, or long-term motor recovery. Longitudinal behavioral assessment using task-specific assays, such as the cylinder or rotarod tests, will be valuable in future studies. Third, detailed pharmacokinetic analyses and strict molar-equivalent comparisons between free and vesicle-associated P110 were not performed. In addition, a systematic dose-response analysis was not performed; therefore, the dose-response relationship and therapeutic window of Pn-EVs@P110 remain to be established in future studies. In addition, no formal a priori sample size or power calculation was performed, and the relatively small sample sizes used for some endpoints may limit the precision and generalizability of the findings. Fourth, the collagenase-induced model does not fully recapitulate all pathological features of spontaneous ICH, and validation in additional experimental models is warranted. Finally, long-term safety, repeated administration, and dose optimization studies remain necessary before translational application can be considered.

Conclusion

Overall, our results indicate that engineered *Panax notoginseng*-derived extracellular vesicle-like nanovesicles can enhance peptide delivery and improve the therapeutic efficacy of P110 in experimental ICH. By integrating pharmaceutical characterization, multi-omics profiling, and mechanistic validation, these findings support the development of plant-derived EV-based delivery platforms for neurological disorders and provide a framework for further exploration of engineered plant vesicles as therapeutic systems.

DECLARATIONS

Acknowledgments

The Graphical Abstract was created in BioRender. Chen, B. (2026) https://BioRender.com/bh89y4d.

Authors' contributions

Made substantial contributions to the conception and design of the study: Chen B, Jiang P
Performed data acquisition, *in vitro* and *in vivo* experiments, and drafted the manuscript: Li Y, Xu B, Sun W
Performed transcriptomic and metabolomic data analysis and interpretation: Zhang T
Established the animal models and provided technical support: Wang C
Performed data analysis and manuscript revision: Chen B, Jiang P
All authors read and approved the final manuscript.

Availability of data and materials

The datasets generated and analyzed during the current study are available from the corresponding author upon reasonable request.

AI and AI-assisted tools statement

Not applicable.

Financial support and sponsorship

This work was supported by Shandong Provincial Natural Science Foundation (ZR2024QH387), Key R&D Program of Jining (2023YXNS226 and 2023YXNS003), and Projects of Medical and Health Technology Development Program in Shandong Province (202502051283).

Conflicts of interest

All authors declared that there are no conflicts of interest.

Ethical approval and consent to participate

All animal experimental procedures were approved by the Animal Ethics Committee of Jining No. 1 People's Hospital (Approval No. JNRM-2025-DW-140) and were conducted in accordance with the Laboratory Animal Environment and Facilities (GB 14925-2010) and the Animal Research: Reporting of *In Vivo* Experiments (ARRIVE) 2.0 guidelines.

Consent for publication

Not applicable.

Copyright

© The Author(s) 2026.

Supplementary Materials

Supplementary Materials

REFERENCES

1. Matsuzaka Y, Yashiro R. Extracellular vesicles as novel drug-delivery systems through intracellular communications. *Membranes*. 2022;12:550. DOI PubMed PMC

2. Sharma S, Masud MK, Kaneti YV, et al. Extracellular vesicle nanoarchitectonics for novel drug delivery applications. *Small.* 2021;17:e2102220. DOI PubMed
3. Jiang L, Vader P, Schiffelers RM. Extracellular vesicles for nucleic acid delivery: progress and prospects for safe RNA-based gene therapy. *Gene Ther.* 2017;24:157-66. DOI PubMed
4. Kim HI, Park J, Zhu Y, Wang X, Han Y, Zhang D. Recent advances in extracellular vesicles for therapeutic cargo delivery. *Exp Mol Med.* 2024;56:836-49. DOI PubMed PMC
5. Xu G, Jin J, Fu Z, et al. Extracellular vesicle-based drug overview: research landscape, quality control and nonclinical evaluation strategies. *Signal Transduct Target Ther.* 2025;10:255. DOI PubMed PMC
6. Lundy DJ, Chau ZL, Chen SY, et al. Beyond extracellular vesicle (EV) hype: practical solutions and remaining hurdles in EV research, manufacturing, and clinical translation. *Adv Sci.* 2026;13:e21913. DOI PubMed PMC
7. Zhang J, Pan Y, She P, Rao L. From bench to bedside: the promise and roadblocks of extracellular vesicle therapeutics. *Theranostics.* 2026;16:5044-64. DOI PubMed PMC
8. Wang Y, Zhao K, Shi X, et al. Plant-derived extracellular nanovesicles for disease therapy. In: Wang Q, Zheng L, Editors. Extracellular vesicles. Singapore: Springer Nature; 2024. pp. 489-511. DOI
9. Alzahrani FA, Khan MI, Kameli N, Alsahafi E, Riza YM. Plant-derived extracellular vesicles and their exciting potential as the future of next-generation drug delivery. *Biomolecules.* 2023;13:839. DOI PubMed PMC
10. Kang SJ, Rhee WJ. Engineered plant-derived extracellular vesicles as targeted drug carriers in cancer therapy. *ACS Appl Bio Mater.* 2026;9:1053-63. DOI PubMed
11. Yazdanpanah S, Romano S, Valentino A, Galderisi U, Peluso G, Calarco A. Plant-derived exosomes: carriers and cargo of natural bioactive compounds: emerging functions and applications in human health. *Nanomaterials.* 2025;15:1005. DOI PubMed PMC
12. Tan F, Liu W, Li T, et al. Plant-derived extracellular vesicles as tools and targets for inflammatory diseases. *J Nanobiotechnology.* 2026;24:397. DOI PubMed PMC
13. Zuo Y, Zhang J, Sun B, et al. A new perspective on regenerative medicine: plant-derived extracellular vesicles. *Biomolecules.* 2025;15:1095. DOI PubMed PMC
14. Zhang J, Tian S, Guo L, Zhao H, Mao Z, Miao M. Chinese herbal medicine-derived extracellular vesicles as novel biotherapeutic tools: present and future. *J Transl Med.* 2024;22:1059. DOI PubMed PMC
15. Chen BB, Wang Y, Li YN, et al. Neuroprotective effects of *Salvia Miltiorrhiza*-derived extracellular nanovesicles in traumatic brain injury. *J Neurotrauma.* 2026;43:295-316. DOI PubMed
16. Wu J, Chen X, Lin X, et al. Protective effects of Panax notoginseng saponins on cerebral ischemia/reperfusion injury: insights into SIRT1/NRF2/HO-1 pathway activation. *Physiol Res.* 2025;74:313-26. DOI PubMed PMC
17. Qu J, Xu N, Zhang J, Geng X, Zhang R. Panax notoginseng saponins and their applications in nervous system disorders: a narrative review. *Ann Transl Med.* 2020;8:1525. DOI PubMed PMC
18. Zhao C, Fu J, Wang Y, Zhou Y. Latest evidence and perspectives of Panax notoginseng extracts and preparations for the treatment of cardiovascular diseases. *J Cardiovasc Pharmacol.* 2025;85:248-60. DOI PubMed
19. Peng M, Yi YX, Zhang T, Ding Y, Le J. Stereoisomers of saponins in *Panax notoginseng* (Sanqi): a review. *Front Pharmacol.* 2018;9:188. DOI PubMed PMC
20. Yang X, Yi R, Tian Y, et al. Effects of stem cell exosomes and sanqi-derived exosome-like nanoparticles on oxidative stress in skin cells. *J Clin Med Images Case Rep.* 2025;5:1797. Available from: https://jcmimagescasereports.org/article/JCM-V5. [Last accessed on 10 Oct 2026].
21. Li S, Zhang R, Wang A, et al. Panax notoginseng: derived exosome-like nanoparticles attenuate ischemia reperfusion injury via altering microglia polarization. *J Nanobiotechnology.* 2023;21:416. DOI PubMed PMC
22. Feigin VL, Brainin M, Norrving B, et al. World stroke organization: global stroke fact sheet 2025. *Int J Stroke.* 2025;20:132-44. DOI PubMed PMC
23. GBD 2019 Stroke Collaborators. Global, regional, and national burden of stroke and its risk factors, 1990-2019: a systematic analysis for the Global Burden of Disease Study 2019. *Lancet Neurol.* 2021;20:795-820. DOI PubMed PMC
24. Lee TH. Intracerebral hemorrhage. *Cerebrovasc Dis Extra.* 2025;15:1-8. DOI PubMed PMC
25. O'Carroll CB, Brown BL, Freeman WD. Intracerebral hemorrhage: a common yet disproportionately deadly stroke subtype. *Mayo Clin Proc.* 2021;96:1639-54. DOI PubMed
26. Gong Y, Li H, Cui H, Gong Y. Microglial mechanisms and therapeutic potential in brain injury post-intracerebral hemorrhage. *J Inflamm Res.* 2025;18:2955-73. DOI PubMed PMC
27. Huang Q, Yu X, Fu P, et al. Mechanisms and therapeutic targets of mitophagy after intracerebral hemorrhage. *Heliyon.* 2024;10:e23941. DOI PubMed PMC

28. Chen W, Guo C, Huang S, et al. MitoQ attenuates brain damage by polarizing microglia towards the M2 phenotype through inhibition of the NLRP3 inflammasome after ICH. *Pharmacol Res.* 2020;161:105122. DOI PubMed
29. Chen T, Gao X, Chang Y, et al. Mitochondrial dysfunction in intracerebral hemorrhage: molecular mechanisms and pathological consequences. *Front Cell Neurosci.* 2026;20:1913984. DOI PubMed PMC
30. Yin R, Qiu C, Shen Q, Wang Z. Corin inhibits microglial inflammatory activation by suppressing mitochondrial dysfunction in intracerebral hemorrhage. *BMB Rep.* 2026;59:143-50. DOI PubMed PMC
31. Liu M, Li B, Yin Z, et al. Targeting mitochondrial dynamics: a promising approach for intracerebral hemorrhage therapy. *Life Sci.* 2025;361:123317. DOI PubMed
32. Reddy PH, Reddy TP, Manczak M, Calkins MJ, Shirendeb U, Mao P. Dynamin-related protein 1 and mitochondrial fragmentation in neurodegenerative diseases. *Brain Res Rev.* 2011;67:103-18. DOI PubMed PMC
33. Shi W, Tan C, Liu C, Chen D. Mitochondrial fission mediated by Drp1-Fis1 pathway and neurodegenerative diseases. *Rev Neurosci.* 2023;34:275-94. DOI PubMed
34. Qi X, Qvit N, Su YC, Mochly-Rosen D. A novel Drp1 inhibitor diminishes aberrant mitochondrial fission and neurotoxicity. *J Cell Sci.* 2013;126:789-802. DOI PubMed PMC
35. Liu W, Su C, Qi Y, Liang J, Zhao L, Shi Y. Brain-targeted heptapeptide-loaded exosomes attenuated ischemia-reperfusion injury by promoting the transfer of healthy mitochondria from astrocytes to neurons. *J Nanobiotechnology.* 2022;20:242. DOI PubMed PMC
36. Shang T, Kuang B, Zheng L, et al. Mitochondrial quality control: insights into intracerebral hemorrhage. *Cell Mol Neurobiol.* 2025;45:79. DOI PubMed PMC
37. Wang M, Wang W, Chopp M, Zhang ZG, Zhang Y. Therapeutic and diagnostic potential of extracellular vesicle (EV)-mediated intercellular transfer of mitochondria and mitochondrial components. *J Cereb Blood Flow Metab.* 2026;46:289-305. DOI PubMed PMC
38. Manickam DS, Pinky PP, Khare P. Extracellular vesicle-mediated mitochondria delivery: Premise and promise. *J Cereb Blood Flow Metab.* 2026;46:306-21. DOI PubMed PMC

Disclaimer/Publisher's Note: All statements, opinions, and data contained in this publication are solely those of the individual author(s) and contributor(s) and do not necessarily reflect those of OAE and/or the editor(s). OAE and/or the editor(s) disclaim any responsibility for harm to persons or property resulting from the use of any ideas, methods, instructions, or products mentioned in the content.



© The Author(s) 2026. Open Access This article is licensed under a Creative Commons Attribution 4.0 International License (https://creativecommons.org/licenses/by/4.0/), which permits unrestricted use, sharing, adaptation, distribution and reproduction in any medium or format, for any purpose, even commercially, as long as you give appropriate credit to the original author(s) and the source, provide a link to the Creative Commons license, and indicate if changes were made.